pISSN 2384-1095
eISSN 2384-1109

iMRI 2021;25:141-155

https://doi.org/10.13104/imri.2021.25.3.141

iMRI
Investigative Magnetic Resonance Imaging

High Resolution 3D Magnetic Resonance Fingerprinting with Hybrid Radial-Interleaved EPI Acquisition for Knee Cartilage T_1, T_2 Mapping

Dongyeob Han[1], Taehwa Hong[1], Yonghan Lee[2], Dong-Hyun Kim[1]

[1]School of Electrical and Electronic Engineering, Yonsei University, Seoul, Korea
[2]Department of Radiology, Research Institute of Radiological Science, Yonsei University College of Medicine, Seoul, Korea

Original Article

Received: April 26, 2021
Revised: April 26, 2021
Accepted: May 15, 2021

Correspondence to:
Dong-Hyun Kim, Ph.D.
Department of Electrical and Electronic Engineering, Engineering Hall 3, Room C228, Yonsei University, 50, Yonsei-ro, Seodaemun-gu, Seoul 03722, Korea.
Tel. +82-2-2123-5874
Fax. +82-2-313-2879
E-mail: donghyunkim@yonsei.ac.kr

Purpose: To develop a 3D magnetic resonance fingerprinting (MRF) method for application in high resolution knee cartilage PD, T_1, T_2 mapping.
Materials and Methods: A novel 3D acquisition trajectory with golden-angle rotating radial in k_{xy} direction and interleaved echo planar imaging (EPI) acquisition in the k_z direction was implemented in the MRF framework. A centric order was applied to the interleaved EPI acquisition to reduce Nyquist ghosting artifact due to field inhomogeneity. For the reconstruction, singular value decomposition (SVD) compression method was used to accelerate reconstruction time and conjugate gradient sensitivity-encoding (CG-SENSE) was performed to overcome low SNR of the high resolution data. Phantom experiments were performed to verify the proposed method. *In vivo* experiments were performed on 6 healthy volunteers and 2 early osteoarthritis (OA) patients.
Results: In the phantom experiments, the T_1 and T_2 values of the proposed method were in good agreement with the spin-echo references. The results from the *in vivo* scans showed high quality proton density (PD), T_1, T_2 map with EPI echo train length (N_{ETL} = 4), acceleration factor in through plane (R_z = 5), and number of radial spokes (N_{spk} = 4). In patients, high T_2 values (50-60 ms) were seen in all transverse, sagittal, and coronal views and the damaged cartilage regions were in agreement with the hyper-intensity regions shown on conventional turbo spin-echo (TSE) images.
Conclusion: The proposed 3D MRF method can acquire high resolution (0.5 mm^3) quantitative maps in practical scan time (~ 7 min and 10 sec) with full coverage of the knee (FOV: 160 × 160 × 120 mm^3).

Keywords: MR fingerprinting; Three-dimensional; High resolution; T_1; T_2; Knee cartilage

INTRODUCTION

Magnetic resonance fingerprinting (MRF) is a novel technique that allows fast simultaneous proton density (PD), T_1, T_2 mapping (1). The key concepts of MRF can be explained in three parts: (1) generating unique signal evolution *via* the fingerprints of tissues using varying flip angles (FA) and repetition times (TR), (2) enforcing incoherent noise achieved by highly undersampling acquisition in random fashion through time,

and (3) pattern matching using the so-called dictionary which contains all possible quantitative *in vivo* entries. These concepts give a new opportunity of 'transient imaging' instead of conventional MR imaging which is based on 'steady-state imaging'. Many variations of MRF have been developed regarding the issues of echo formalism (2, 3), reconstruction method (4-7), B_1 inhomogeneity compensation (8-10), extending parameters (11-13), applications (14-16), to name a few. Most of the previous studies, however, were focused on (multi-slice) 2D image acquisition.

Development of 3D MRF can enable volumetric quantitative mapping with higher through plane resolution without gaps but is challenging due to the prolonged scan time (8, 17). The main concern in 3D MRF is filling the volumetric k-space effectively since multiple MRF acquisition groups for the slice (or volumetric) encoding with waiting time between every two MRF acquisition groups is necessary. Recently, several 3D MRF techniques have been developed with consideration of reducing the number of acquisition groups (18-21). For instance, the stack-of-spiral acquisition with a uniform undersampling in the through plane was applied with generalized autocalibrating partial parallel acquisition (GRAPPA) reconstruction (18). Another stack-of-spiral 3D MRF used k_z-t undersampling which could increase noise incoherency in the fingerprints (19, 21). A 3D MRF technique with rotating spiral trajectory on multi-axis reduced the MRF acquisition group substantially (20).

One important clinical application of 3D quantitative imaging is osteoarthritis (OA) diagnosis in cartilage of the knee. Many T_1 and T_2 mapping techniques in clinical OA studies have been reported because the quantitative values were related with the compositional status of the cartilage (22-25). The T_2 values refer to the water content changes in the extracellular matrix of articular cartilage. Thus, clinical studies reported that the increase of T_2 values were observed in damaged cartilage (26-32). Another well validated quantification method in OA is delayed T_1 mapping with injection of the contrast agent, namely, gadolinium diethylene triamine pentaacetic acid ($Gd(DTPA)^{2-}$) called dGEMRIC (33-36). The measurements of T_1 values with $Gd(DTPA)^{2-}$ correlate with glycosaminoglycan concentration (GAG) indirectly. Despite the clinical importance of acquiring quantification map in cartilage, T_1 and T_2 mappings are limited by the long scan time and relative low resolution. Furthermore, T_2 mapping has morphological discontinuity due to the gap of the 2D multi-slice acquisition. In addition, the chemical shift effect of fat also needs to be addressed.

The application of 3D MRF for articular cartilage has strong clinical significance but is challenging due to the morphological characteristic of knee cartilage which requires less than a few millimeters thickness. Two previous methods mentioned above presented sub-millimeter resolution 3D MRF. Ma et al. (21) showed 3D MRF with 0.6 mm isotropic resolution achieved by 2× interpolation from the original 1.2 mm isotropic resolution acquisition while Cao et al. (20) enabled 0.8 mm isotropic resolution 3D MRF. These 3D MRF studies, however, have been applied mainly for brain imaging. For MSK applications, one previous MRF study reported hip articular cartilage with in-plane voxel size 0.6 × 0.6 mm (2, 37). Radial trajectory was used to acquire high in-plane resolution T_1, T_2 maps with 2D multi-slice acquisition.

In this study, we proposed a method for high resolution 3D MRF of knee cartilage scanned within clinically acceptable time. To overcome the challenges induced by achieving both high resolution mapping and practical scan time, the proposed method was developed in two aspects. First, a novel pulse sequence was proposed with 3D hybrid radial-interleaved echo planar imaging (EPI) acquisition in MRF framework. The proposed acquisition trajectory acquired data with radial acquisition in the in-plane while simultaneously applying interleaved EPI in the through plane. In addition, a centric order was applied in the EPI acquisition to mitigate Nyquist ghosting artifact due to the off-resonance caused by fat. Second, for the reconstruction, a singular value decomposition (SVD) compression method (4) was used to accelerate reconstruction time. Furthermore, CG-SENSE method (38, 39) was applied after the SVD compression to overcome the signal to noise ratio (SNR) problem due to the high resolution acquisition. These improvements in both pulse sequence and reconstruction allowed 3D parameter mapping at 0.5 mm isotropic resolution with a whole knee cartilage coverage (160 × 160 × 120 mm^3) in 7 min and 10 sec. The proposed method was validated with phantom and *in vivo* experimentation of two patients.

METHODS

Pulse Sequence Development

Part of the pulse sequence diagram is shown in Figure 1. A 3D slab-selective MRF with fast imaging with steady-state precession (FISP) (2, 19) was developed with a 3D

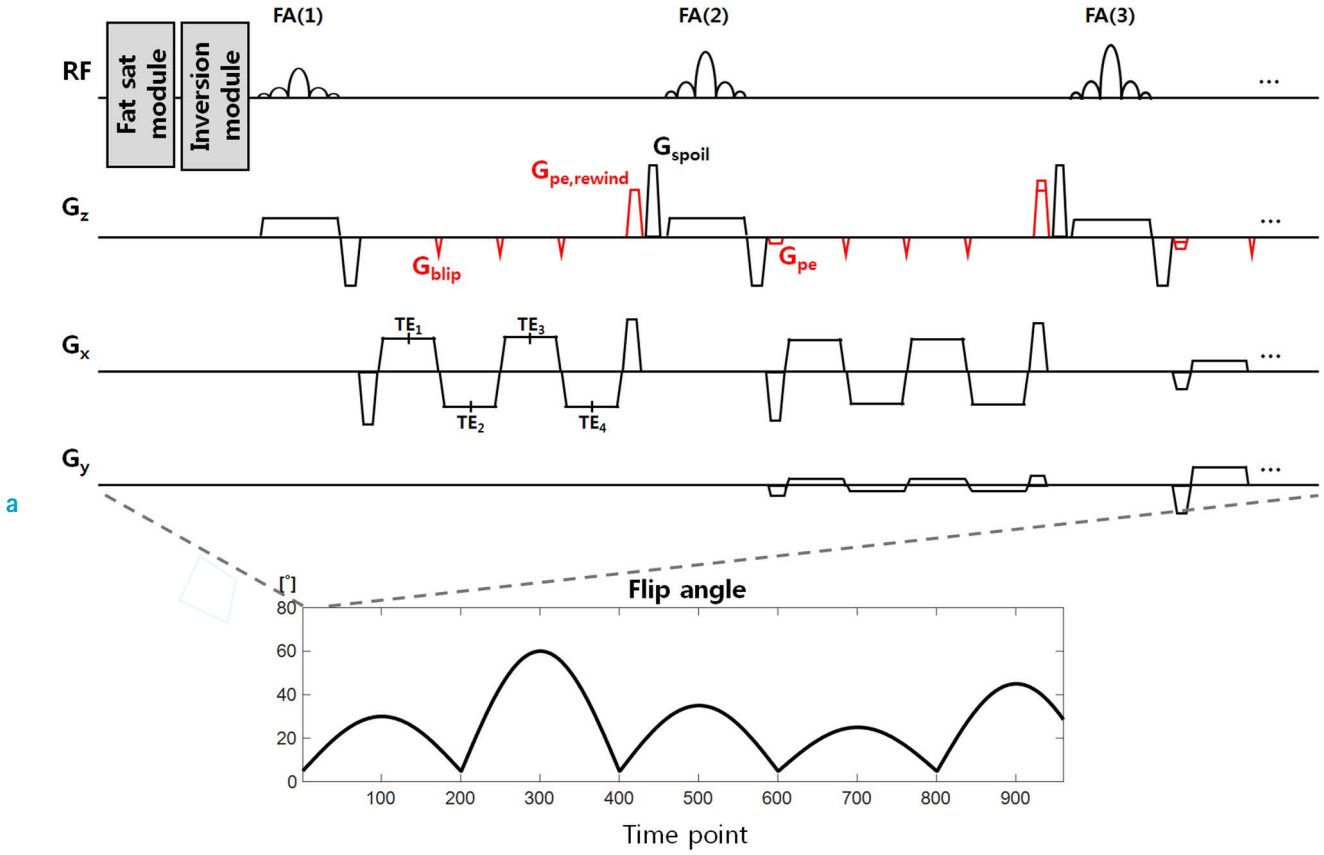

Fig. 1. (a) Proposed pulse sequence diagram during the first three flip angles with four echo train length (N_{ETL} = 4). The gradients for EPI acquisition in through plane (red), G_{blip}: gradient for the EPI blip, G_{pe}: gradient for partition encoding which varies through the time points, and $G_{pe,rewind}$: rewind gradient for the zero moment before the spoiler gradient (G_{spoil}). (b) The 960 sinusoidal flip angle patterns used in this study.

acquisition trajectory-a hybrid radial-interleaved EPI acquisition. The hybrid radial-interleaved EPI trajectory collects data with radial k-space acquisition in in-plane (k_{xy}) while moving through the through plane (k_z) in an interleaved fashion.

The proposed radial-interleaved EPI was designed as following: (1) N_{ETL} (echo train length) radial spokes in the k_z-axis with different partition encoding acquired in each TR, (2) blip gradient set to have moment $k_{z,blip} = \pm k_{z,max}/N_{ETL} = \pm(\Delta k_z\ N_z/2)/N_{ETL}$ where N_z is the total number of acquired slices, (3) centric ordering, i.e., one interleaf only covers half of k_z domain, (4) radial interleaf rotated with golden angle at each time point (40), (5) k-t uniform under sampling applied in k_z partitions in an interleaved fashion same as the previously proposed 3D MRF method (19).

A total of 960 sinusoidal flip angles were used to generate MRF signal as shown in Figure 1b. Constant TR was used to minimize scan time similar to other 3D MRF studies (18-20). Fat saturation module was applied every 20th RF (or time point) to reduce fat signal and partial volume effect (16). Non-selective adiabatic inversion pulse was also applied before the 1st excitation pulse as shown in Figure 1a. Spoiling gradient (G_{spoil}) was set to have 2π dephasing.

To fill the 3D MRF k-space, the MRF acquisition with 960 sinusoidal flip angles were repeated N_{acq} times similar to other 3D MRF studies (18-20). N_{acq} was defined as the product of the number of radial spokes (N_{spk}) used to fill in-plane and the number of interleaves (N_{int}) used to cover the through-plane at each time point. The number of interleaves, N_{int}, was calculated by $N_{int} = N_z/(N_{ETL} \cdot R_z)$ where R_z is an acceleration factor in k_z-t domain.

An example of the proposed 3D MRF acquisition is shown in Figure 2. In this figure, we assumed that a total of 80 slices (N_z = 80) were acquired with N_{ETL} = 4, R_z =

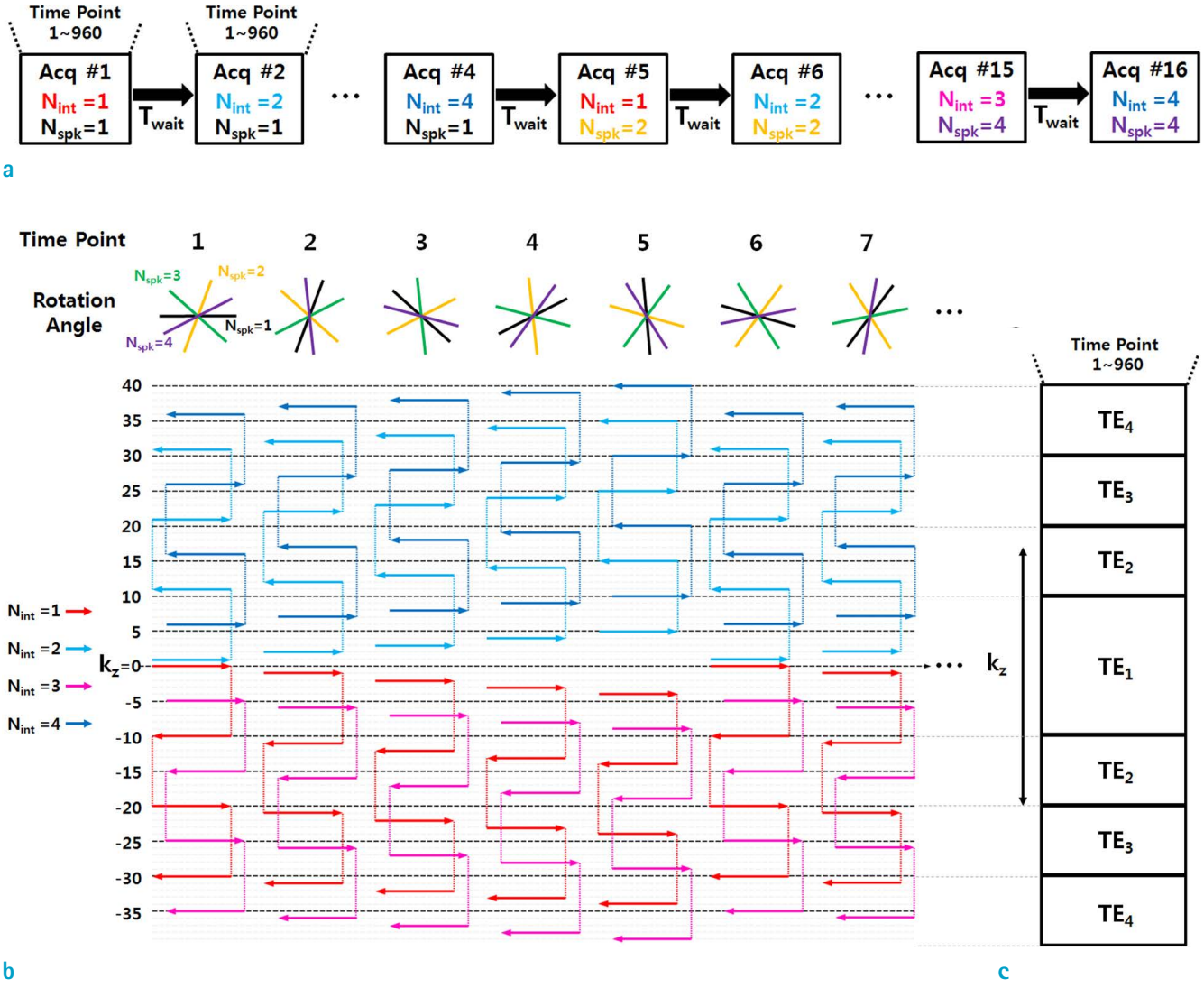

Fig. 2. An example of the acquisition sequence and trajectories of the proposed MRF with the parameters N_z = 80, N_{ETL} = 4, N_{spk} = 4, R_z = 5. All the line colors in (a) and (b) were synchronized. (a) Each MRF acquisition group contains 960 flip angles. Waiting time (T_{wait}) was set to 2 sec. (b) Acquisition trajectories in each group for the proposed method. (c) A k_z space map with respect to the acquired echo time of the EPI acquisition. The shortest echo time data was collected in 25% ($1/N_{ETL}$) of the center in k_z-axis.

5. Therefore, 4 interleaves (N_{int} = 80/(4·5) = 4) covered k_z axis at each MRF time point. For in-plane domain, 4 radial spokes (N_{spk} = 4) were assumed. As a result, 16 (= N_{int}·N_{spk}) MRF acquisition groups were repeated as shown in Figure 2a. For T_1 recovery, the waiting time between MRF acquisition groups (T_{wait}) was set to 2 sec.

The k-space trajectories of the proposed method in each MRF acquisition group are plotted in Figure 2b. In the first acquisition group, e.g., data were collected following the red EPI lines along the black rotation angles. The red EPI lines with descending order acted in an undersampled k_z-t interleave fashion as depicted in this case (R_z = 5). Afterwards, at the 6th time point, the red EPI lines started at the same partition encoding as the 1st time point but with different rotation angle. This pattern continued until the 960th time points. Because centric order was used for the next interleaf (N_{int} = 2), the blue EPI lines were used in ascending order starting at k_z = 1, and so forth. Finally, these hybrid radial-interleaved EPI patterns with varying 960 flip angles (or time points) were repeated N_{spk} times with golden angle rotation as shown in Figure 2a and b. A k_z-space map of the proposed method with respect to

the acquired echo time is shown in Figure 2c. Because centric ordering was used, $1/N_{ETL}$ center portion of k_z-axis had the same shortest echo time (TE_1). This acquisition pattern mitigated Nyquist ghosting artifact due to the field inhomogeneity and chemical shift of fat (41).

Dictionary Generation

The dictionary for the matching was generated based on the Bloch equation in MATLAB (The MathWorks, Natick, MA, USA). Only water molecules were considered in this study since fat saturation module was used in the acquisition. The insufficient T_1 recovery of the longitudinal magnetization due to the 2 sec waiting time was incorporated in the simulation. A total of 501 isochromats were simulated. The study conducted by Ma et al. (19) provided more details regarding waiting time consideration and multiple isochromats. The T_1 range of the dictionary was 150 to 2000 ms with 10 ms step size and 2050 to 3000 ms with 50 ms step size. The T_2 range was 5 to 250 ms with 1 ms step size and 260 to 350 ms with 10 ms step size.

Reconstruction

Two reconstruction methods were combined, namely, MRF-SVD compression to reduce the reconstruction time (4, 19) and CG-SENSE parallel imaging to overcome low SNR (39). The reconstruction pipeline is shown in Figure 3. Details of reconstruction process are described below:

Step 1. Data acquisition

The acquired data size using the proposed sequence was $S \in C^{Nt \times M}$, $M = N_c \times N_{read} \times N_{Nyqspk} \times N_z$ where S is the acquired MRF raw data, N_t is the time point of MRF signal (960 in this study), N_c is the number of coils, N_{read} is the readout sampling number, and NNyqspk is the N_{yquist} sampling number of radial spokes.

Step 2. SVD compression in k-space domain

The dictionary, $D \in C^{N_t \times N_{atom}}$ where N_{atom} is the total number of combinations of T_1 and T_2 values, was compressed using singular value decomposition method (4).

$$D = U\Sigma V^* \approx U_{N_{sv}} \Sigma_{N_{sv}} V^*_{N_{sv}}$$
$$\tilde{D} = U^*_{N_{sv}} D$$

where $U^*_{N_{sv}} \in C^{N_{sv} \times N_t}$ is the first N_{sv} of the left singular vector of the dictionary and the compressed dictionary became $\tilde{D} \in C^{N_{sv} \times N_{atom}}$. The first five singular vectors ($N_{sv} = 5$) were used in this study because they had 99% power of the signal. Then the SVD compressed MRF signal was obtained by

$$\tilde{S} = U^*_{N_{sv}} S$$

where $\tilde{S} \in C^{N_{sv} \times M}$.

Step 3. Sensitivity map estimation using ESPIRiT from 1st SVD compressed k-space

Since the 1st singular value contained most of the energy, the first SVD compressed data was used for the sensitivity map estimation using ESPIRiT (42). A total of 15 channel sensitivity maps with knee coil were estimated.

Step 4. CG-SENSE reconstruction

To overcome low SNR due to high resolution acquisition and high acceleration factor, CG-SENSE with Tikhonov regularization was applied (39, 43). The problem can be stated as

$$\tilde{x}(n) = \arg\min_{\tilde{x}(n)} \sum_c ||G \cdot F \cdot \widetilde{E_c} \cdot \tilde{x}(n) - \tilde{S}(n)||_2^2 + \lambda ||\tilde{x}(n)||_2^2,$$
$$n = 1, 2, \ldots N_{SV}$$

where G·F is the NUFFT operator, $\widetilde{E_c}$ is the sensitivity map acquired from step 3, $\tilde{S}(n)$ is the n^{th} SVD compressed acquired data, $\tilde{x}(n)$ is the reconstructed n^{th} SVD compressed MRF data, and λ (set as 1) is the regularization factor.

Step 5. SVD compressed dictionary matching

Finally, reconstructed MRF images ($\tilde{x}(n)$) were matched with SVD compressed dictionary ($\tilde{D}$). Matching was performed *via* the inner product.

The implementation of steps 3 and 4 was done by the Berkeley Advanced Reconstruction Toolbox (BART) (44). All the other computations were performed using MATLAB. The whole reconstruction time was about one hour using a Linux server with Core i7 intel Xeon 3.6GHz CPUs and 128GB RAM.

Phantom Experiments

For phantom validation, 7 water vials containing different concentrations of manganese (II) chloride (30, 50, 70, 80, 150, 200, and 350 μM) were prepared. To verify the accuracy and EPI effect of the quantification, MRF scans were performed twice with $N_{ETL} = 1$ (stack-of-star acquisition) and $N_{ETL} = 4$. Scan times were 9 min and 16 sec and 2 min and 19 sec, respectively. Other scan parameters were as follows: field of view (FOV) = 160 × 160 × 40 mm^3,

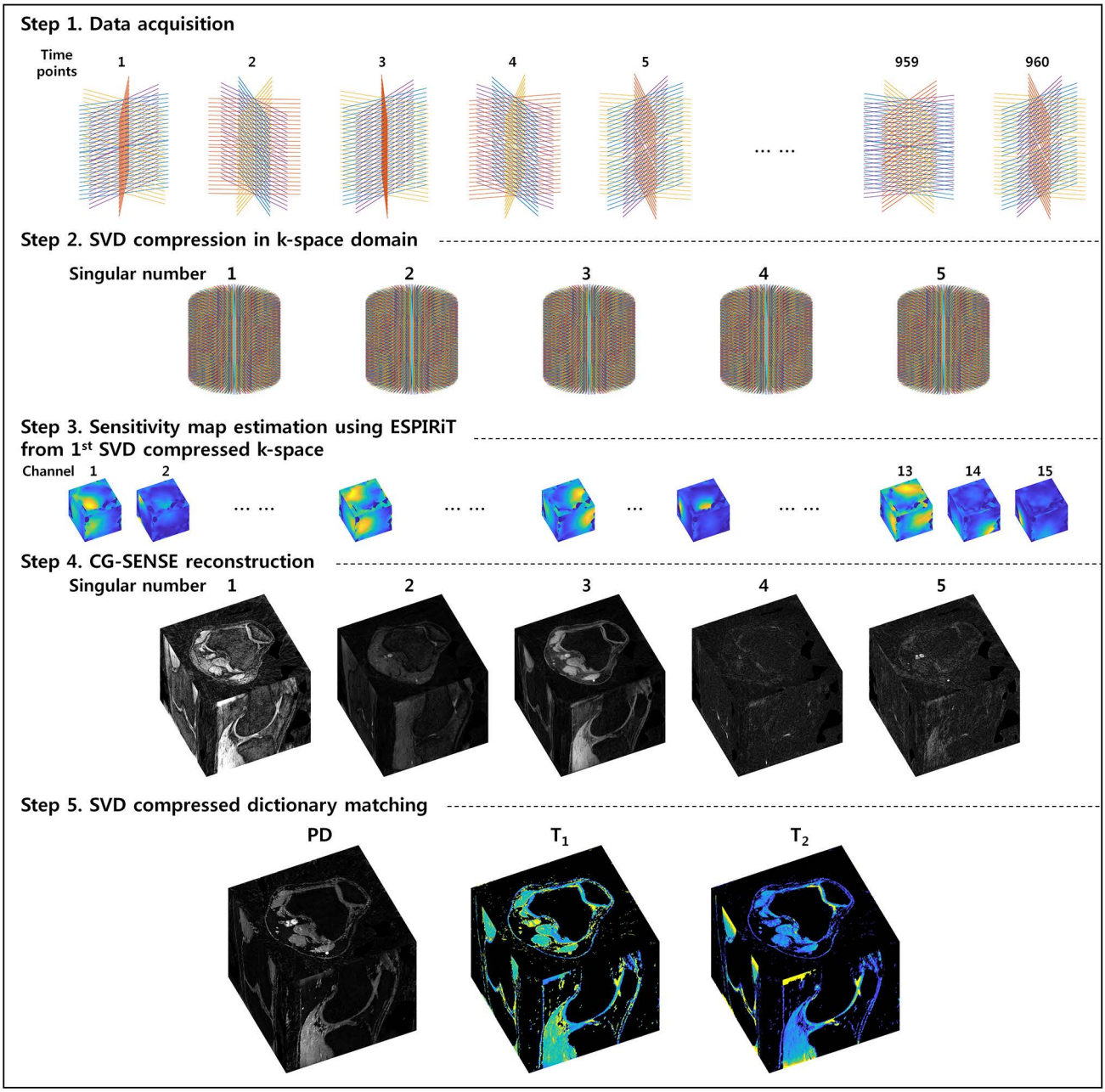

Fig. 3. The reconstruction pipeline of the proposed method. The combined k-space trajectories after all acquisition groups using the proposed method are plotted in Step 1. After the SVD compression in k-space, the 3D k-space data are mostly filled as shown in Step 2. Sensitivity maps estimated using ESPIRiT are shown in Step 3. Reconstructed volumetric singular images using CG-SENSE are shown in Step 4. Finally, quantitative maps after the SVD compressed dictionary matching are shown in Step 5.

resolution = 0.5 × 0.5 × 1 mm^3, 960 sinusoidal FA pattern (Fig. 1c), TR = 16 ms, N_{spk} = 4, R_z = 5, bandwidth = 630 Hz/Px.

For comparison, T_1 and T_2 maps were acquired with gold standard multi-TI inversion-recovery spin echo and multi-TE single-echo spin echo sequences. For inversion-recovery spin echo scans, the scan parameters were as follows: TR = 6000 ms, TE = 10 ms, TI = 50, 100, 200, 400, 800, 1200, and 2400 ms. For multi-TE spin echo scans, the scan parameters were as follows: TR = 6000 ms, TE = 10, 20, 40, 60, 100, 150, 200, and 400 ms. For both scans, FOV was set at 160

× 160 mm^2 with 2.5 × 2.5 mm^2 resolution and 2 mm slice thickness. The total scan time for the gold standard maps was 1 hour and 38 minutes. The T_1 and T_2 values were estimated using non-linear least square fitting.

In vivo Experiments

Because the proposed pulse sequence contained several controllable parameters (e.g., N_{ETL}, N_{spk}, and R_z) that were required for further optimization in an *in vivo* environment, dedicated *in vivo* experiments were performed with 6 healthy volunteers. Furthermore, two patients scans were also performed. All *in vivo* scans were performed with internal review board approval. Common scan parameters for all *in vivo* scans were as follows: FOV = 160 × 160 × 120 mm^3, resolution = 0.5 × 0.5 × 1 mm^3 (interpolated to 0.5 mm isotropic resolution), 960 FAs, bandwidth = 630 Hz/Px, T_{wait} = 2 sec.

The details of the scans for the 6 healthy volunteers were as follows:

1) Comparison of the effect of the proposed EPI acquisition with N_{ETL} = 1, 4, 12. Because of the different ETL, constant TR values were set at 8.1, 16, and 36 ms, respectively. In addition, the intervals of fat saturation module were also changed to 40, 20, and 10 TRs (or time points), respectively, to sustain similar fat T_1 recovery. Other parameters were as follows: N_{spk} = 4, R_z = 5, and scan times were 16 min and 7 sec, 7 min and 10 sec, and 5 min and 2 sec, respectively.
2) Image quality comparison with different number of radial spokes, N_{spk} = 1, 2, 4, 8. Other parameters were set as follows: N_{ETL} = 4, R_z = 5, TR = 16 ms, fat saturation interval = 20. Scan times were 1 min and 48 sec, 3 min and 35 sec, 7 min and 10 sec, and 14 min and 21 sec, respectively.
3) Same scans with and without fat saturation module were performed using the same parameters, N_{ETL} = 4, R_z = 5, N_{spk} = 4, TR = 16 ms. The scan time of the sequence without fat saturation module was 6 min and 57 sec.
4) To validate the SNR improvement of the proposed reconstruction with respect to the direct NUFFT reconstruction, two scans with different through plane acceleration factors (R_z = 3 and 5) were performed. Other parameters were set as follows: N_{ETL} = 4, N_{spk} = 4, TR = 16 ms. The scan time of the scan with R_z = 3 was 11 min and 58 sec.
5) Comparison with conventional T_1, T_2 mapping methods. For the T_1 mapping, DESPOT1 (45) was used with the following scan parameters; resolution = 0.5 × 0.5 × 2 mm^3, TR = 15 ms, TE = 2.5 ms, FA_1 = 4°, FA_2 = 24°, slice partial fourier = 6/8, GRAPPA factor 2. The scan time for DESPOT1 was 5 min. A 2D multi-slice multi-echo spin echo was performed for T_2 mapping with the following scan parameters: resolution = 0.5 × 0.5 mm^2, 50 slices with 20% gap, slice thickness = 2 mm, TR = 4530 ms, TE = 10.5, 21, 31.5 42, 52.5, 63, 73.5, and 84 ms, phase partial fourier = 5/8, GRAPPA factor 2. The scan time of T_2 mapping was 8 min and 52 sec. Voxel-by-voxel fitting was performed, except for the 1st echo, to reduce the stimulated echo effect (46). Scan parameters for the 3D MRF scan were as follows: N_{ETL} = 4, R_z = 5, N_{spk} = 4, TR = 16 ms with 7 min and 10 sec scan time.
6) Repeatability study was performed by 3 successive 3D MRF scans. Scan parameters were same as experiment 5.

Two OA patients' scans were performed with the same scan parameters as in experiment 5. In addition, conventional 2D multi-slice T_2 weighted TSE with fat saturation images were acquired for comparison. The TSE scan was performed with the same FOV and resolution as the MRF scans without gap between slices. Other parameters were TR = 10590 ms, TE = 77 ms, turbo factor = 8, GRAPPA factor 2, NEX = 2 with 6 min and 23 sec scan time. These TSE scans were also acquired in healthy volunteers 1 and 2. All scans were performed in a 3T scanner (Prisma, Siemens Healthcare, Erlangen, Germany) with 15 channel knee coil.

Region of interest (ROI) analysis was also performed over 5 regions including patellar, femoral, tibial cartilage, specific region of damaged cartilage, and muscle. The mean and standard deviation of the T_1 and T_2 values in each region were calculated among all 6 healthy volunteers and the 2 patients.

RESULTS

Figure 4 shows results from the phantom study. Figure 4a shows the images with respect to different N_{ETL} and Figure 4b shows linear regression results of the T_1, T_2 maps for the proposed method with N_{ETL} = 1 and 4 along with the gold standard method. Both maps with different echo train lengths were in good agreement with the T1, T2 maps of the spin echo references (Fig. 4a). Similar results were seen for the linear regression and R^2 values (Fig. 4b), demonstrating that the proposed method provided consistent measurements of the T_1 and T_2 values with the gold standard method in both N_{ETL} = 1 and 4.

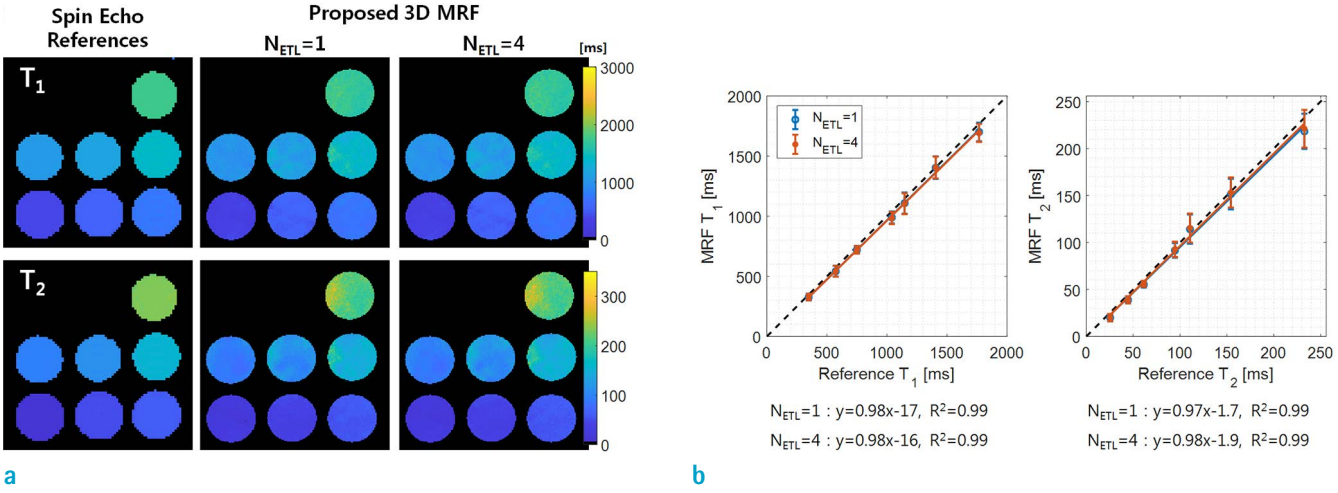

a b

Fig. 4. (a) Comparison of the T_1 and T_2 maps of the phantom experiments using the gold standard method and the proposed 3D MRF method with different parameters (N_{ETL} = 1 and 4). The T_1, T_2 maps of the reference were interpolated from 2.5 × 2.5 mm^2 to 1.25 × 1.25 mm^2. (b) Mean and standard deviation values of T_1 and T_2 values in each vial of the phantom along with the linear regression and R^2 values.

Figure 5 presents the EPI acquisition effect of the proposed method in an *in vivo* environment. The PD, T_1, T_2 maps of the N_{ETL} = 1 and 4 acquisition showed similar results in both axial and sagittal views as shown in Figure 5a and b. However, when N_{ETL} = 12, corrupted images could be seen due to Nyquist ghosting artifact and T_2* effect due to the long echo train length of the EPI acquisition. This shows that echo train length needs to be chosen carefully. The results of N_{ETL} = 4 acquisition showed images without apparent artifacts.

In Supplementary Figure S1, results with different numbers of radial spokes are provided. Increased radial spokes provided improved quality of PD, T_1, T_2 maps as expected. Using 4 radial spokes (N_{spk} = 4) in the proposed acquisition would be a practical choice since imaging could be performed in 10 minutes with similar image quality with N_{spk} = 8 results.

The effect of applying fat saturation module is presented in Supplementary Figure S2. Fat tissues, including the bone and subcutaneous fat, in the PD map with fat saturation were clearly suppressed compared to the PD map without fat saturation. Then, the fat tissues in the T_1, T_2 maps were additionally masked out based on the PD map (PD < 0.2). This additional step was used in *in vivo* T_1, T_2 map results of the study.

The results of two different acquisition (R_z = 3 and 5) with the direct reconstruction (NUFFT) and the proposed method (CG-SENSE) are shown in Figure 6. Because of the small voxel size in the acquisition, noisy quantitative maps were estimated using the SVD and NUFFT reconstruction method with R_z = 3. This became worse with R_z = 5 acquisition due to further acceleration. However, using the CG-SENSE reconstruction, the SNR improvements of the PD, T_1, T_2 maps were clearly seen in both the R_z = 3 and 5 acquisition. Especially, significant image quality improvement was observed in the results of the R_z = 5 using the proposed reconstruction method compared to the direct reconstruction method.

Based on the phantom and *in vivo* experiment results, parameters with N_{ETL} = 4, N_{spk} = 4, R_z = 5 provided acceptable quality maps within a practical scan time (7 min and 10 sec). Further quantitative validation of these parameters is shown in Figure 7 and Supplementary Figure S3.

Figure 7 shows comparison of the T_1 and T_2 maps using the proposed method and the conventional quantitative methods using DESPOT1 and multi-echo spin echo. Slight T_1 underestimation of the proposed method was shown as compared to the T_1 maps using DESPOT1 in Figure 7a, which were also reported in the original MRF study (1). The T_2 map of the proposed method was in good agreement with the T_2 map using the multi-echo spin echo sequence (Fig. 7b).

Results of the repeatability study for *in vivo* experimentation were presented in Supplementary Figure S3. The PD, T_1, T_2 maps of the cartilage region from the first, second, and third scans were shown. Consistent quantitative results within

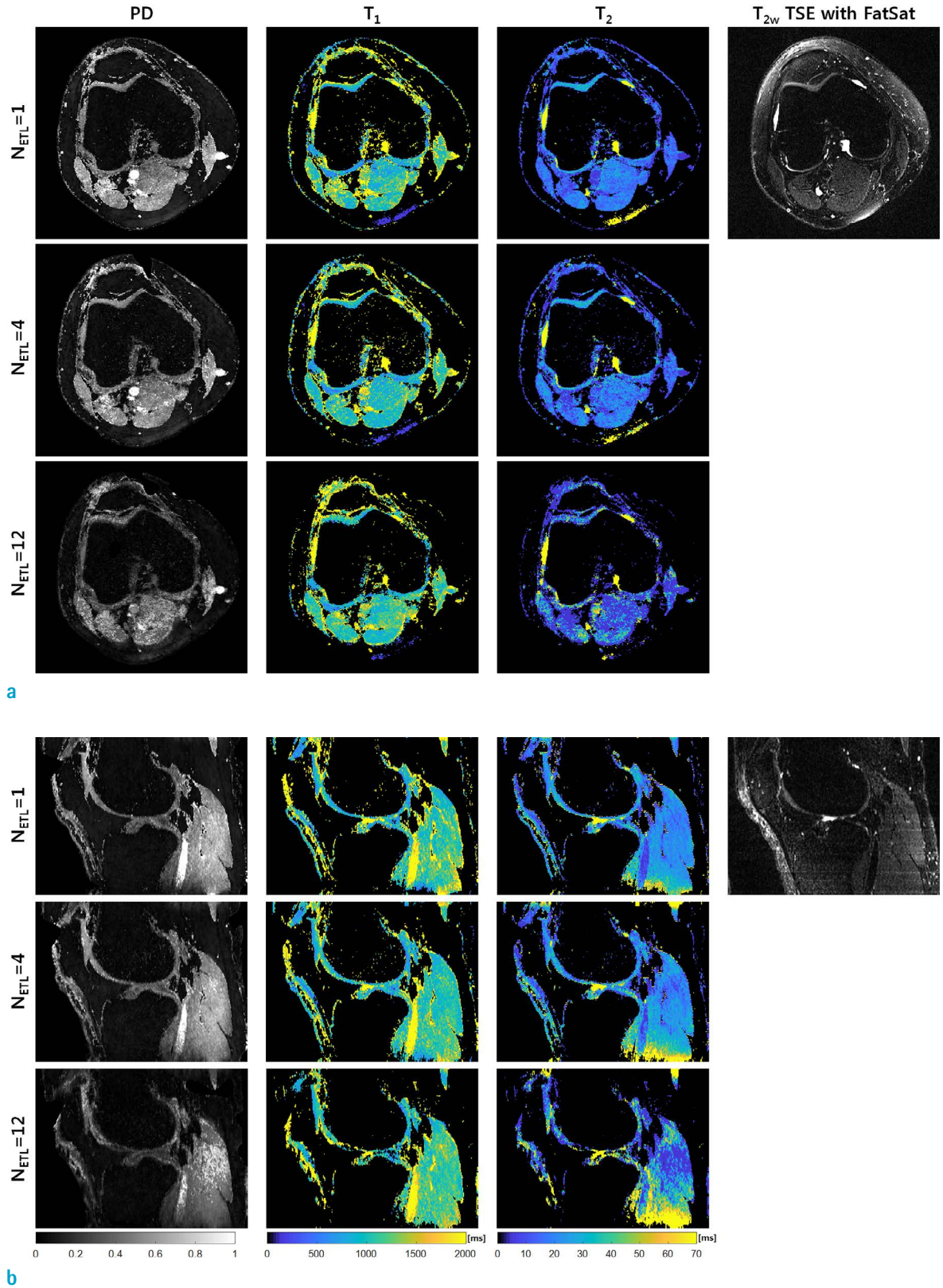

Fig. 5. PD, T_1, T_2 maps using the proposed method with different echo train length acquisition. The N_{ETL} = 1 acquisition was exactly the same as the stack-of-star acquisition. (a) Axial and (b) sagittal views. For morphological comparison, conventional TSE with fat saturation images are also presented (right).

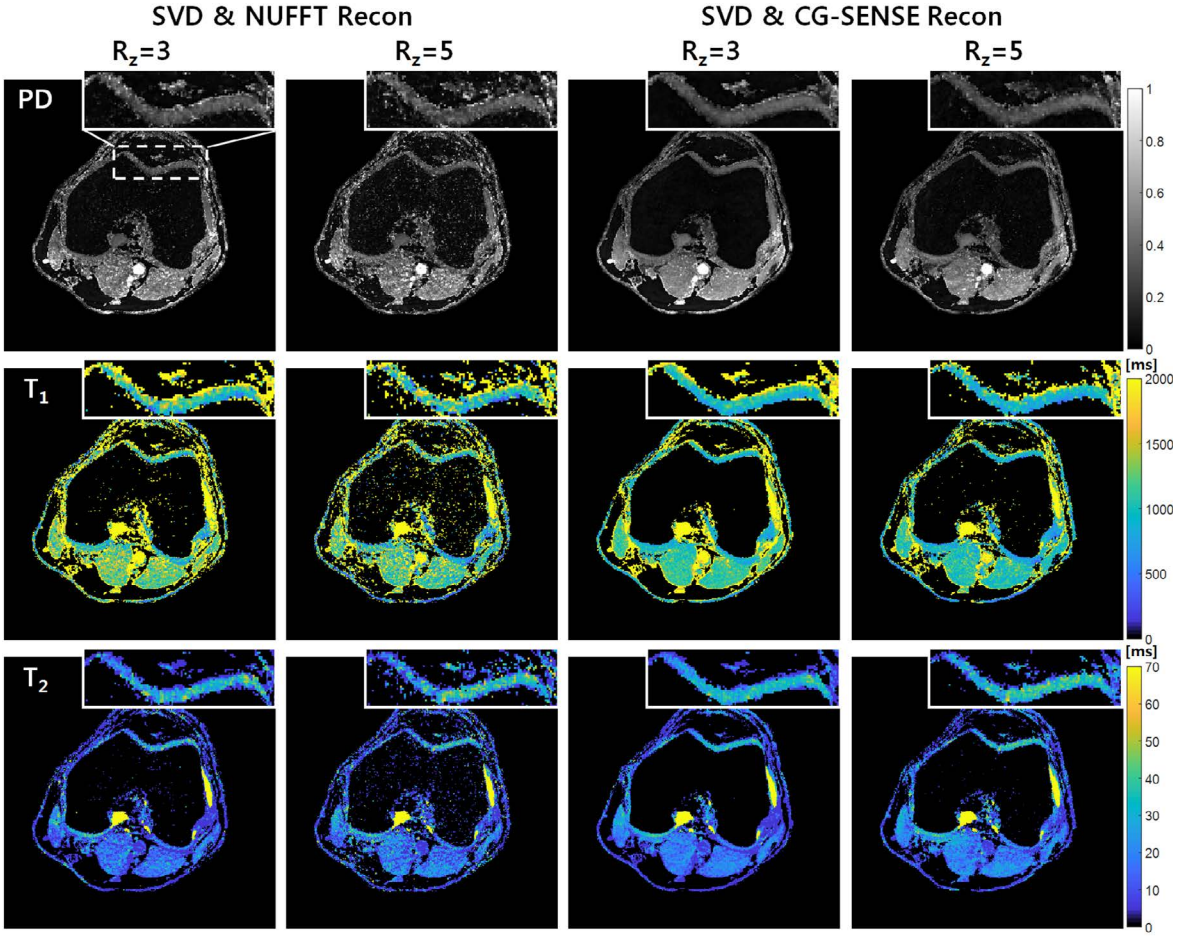

Fig. 6. Axial PD, T_1, T_2 maps from the proposed method with R_z = 3 and 5 acceleration factors. Two different reconstruction methods were compared. Direct reconstruction method (left) and the proposed method using parallel imaging (right) are shown.

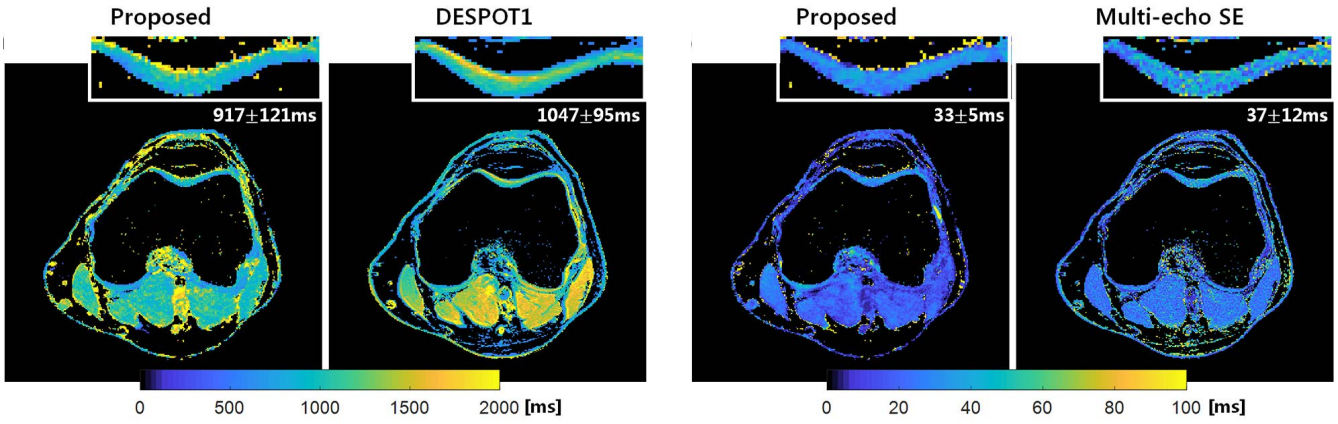

a b

Fig. 7. Quantitative maps from the proposed method with conventional mapping method for comparison. Cartilage region of each map was zoomed with mean and standard values of each quantification (white box). (a) T_1 maps from the proposed method and variable flip angle methods (DESPOT1). (b) T_2 maps from the proposed method and multi-echo spin echo sequence with mono-exponential fitting.

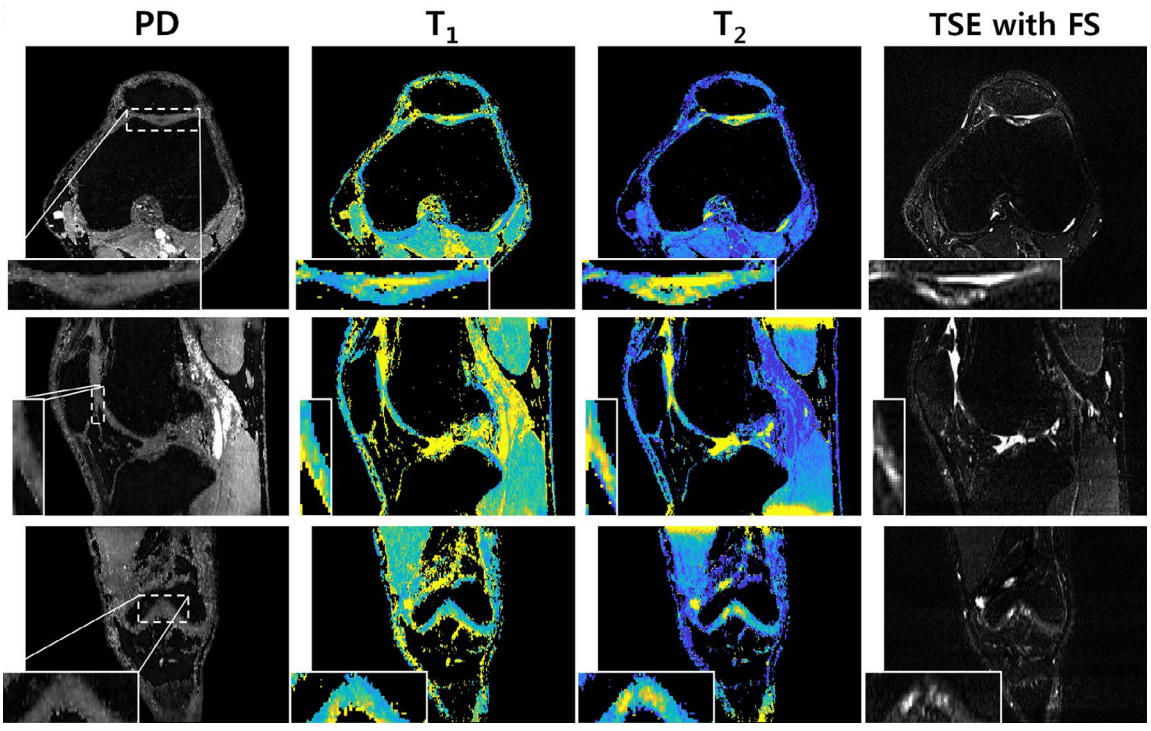

a

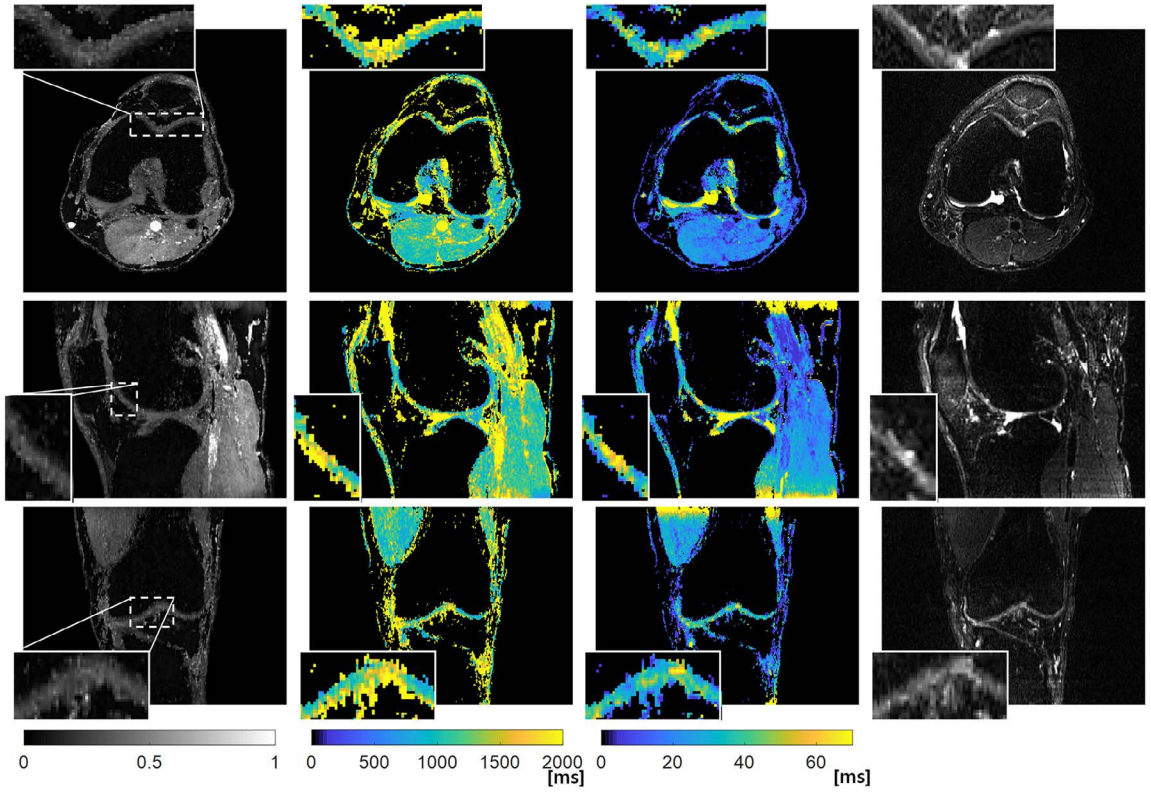

b

Fig. 8. (a, b) Axial, sagittal, and coronal views of PD, T_1, T_2 maps using the proposed method from two patients. Conventional 2D multi-slice TSE with fat saturation is also shown (right). Damaged regions are zoomed (white box).

error boundary of the mean and standard T_1, T_2 values in the red region of interest were measured for the three scans.

Figure 8 shows patients' results for the proposed method. All axial, sagittal, and coronal views of the 3D PD, T_1, T_2 maps were presented. For comparison, conventional T_2 weighted TSE with fat saturation images of all three views were also provided. Patient 1 who has a modified Outerbridge grade II showed cartilage signal change in the femoral trochlea (Fig. 8a) (47). The measured T_2 values with the proposed method increased in the region with cartilage defects. Similar hyper intense TSE images were also seen in these regions. The T_1 values also slightly increased (Fig. 8a). Similar results showing increased T_1 and T_2 values in the damaged region were also seen in the quantitative maps of patient 2 (Fig. 8b). These regions were also in agreement with the region with bright signal in TSE images. The patient 2 was diagnosed with modified Outerbridge grade III in the femoral trochlea.

The ROI analysis of the 5 representative regions from the 6 healthy volunteers and the 2 patients were summarized in Table 1. The T_1, T_2 values from the four regions (patellar, femoral, tibial cartilage, and muscle) were consistent among the 6 healthy volunteers and the 2 patients. In the damaged cartilage region, the increase of both mean and standard deviation values of T_1 and T_2 values could be seen, the latter was due to the increased heterogeneity of the damaged cartilage.

DISCUSSION

In this study, we proposed a 3D high resolution MRF method with hybrid radial-interleaved EPI acquisition. Whole coverage of knee cartilage with isotropic 0.5 mm resolution 3D quantitative maps were achieved in 7 min and 10 sec. Optimization of both pulse sequence and reconstruction helped in achieving the 3D high resolution quantitative map. The proposed method was optimized and validated based on phantom and *in vivo* scans of clinical subjects.

The key contribution of fast and 3D high resolution data acquisition is the hybrid radial-interleaved EPI acquisition with accelerated scheme. Several 2D MRF studies with radial acquisition already showed sub-millimeter resolution quantitative maps (37, 48). Radial MRF can achieve finer resolution than spiral MRF due to its linear path in k-space. To extend to 3D, a simple implementation of stack-of-star in 3D MRF would be less time efficient than the stack-of-spiral 3D MRF because multiple radial spokes might be necessary to fill the in-plane k-space. We overcame this by combining radial and EPI acquisition in a hybrid radial-interleaved EPI acquisition. Therefore, both 3D high resolution and fast acquisition could be achieved simultaneously. However, because of this, slight blurring could occur in the slice direction due to the T_2^* decay during the EPI acquisition.

Another feature of the proposed method is related to centric ordering in the hybrid radial-interleaved EPI acquisition. The centric ordering helps in terms of accurate quantification by providing exact TE values and reducing

Table 1. T_1 and T_2 values (in ms, mean±SD) in the 6 Regions of Interest from the 6 Healthy Volunteers and the 2 Patients

Region		Healthy volunteers							Patients	
		Subject 1	Subject 2	Subject 3	Subject 4	Subject 5	Subject 6	All subjects	Patient 1	Patient 2
Patellar cartilage	T_1	911±139	861±162	958±169	960±149	925±180	897±124	912±157	843±105	835±118
	T_2	29±5	24±6	26±6	27±8	29±7	34±5	28±7	22±5	29±5
Femoral cartilage	T_1	850±140	949±177	942±194	920±150	975±182	998±208	937±176	957±199	920±213
	T_2	33±9	31±7	31±7	29±8	37±8	37±6	33±7	33±6	31±7
Tibial cartilage	T_1	803±126	1124±269	906±194	870±158	857±160	899±155	889±173	861±152	789±155
	T_2	25±7	37±9	25±7	24±7	26±9	32±7	27±8	26±9	24±6
Damaged cartilage	T_1	-	-	-	-	-	-	-	1357±300	1489±457
	T_2	-	-	-	-	-	-	-	59±15	53±12
Muscle	T_1	1067±116	1120±208	1102±119	1087±106	1111±97	1119±127	1102±137	1047±107	1118±124
	T_2	24±4	24±5	22±3	19±3	18±3	26±4	22±4	20±4	23±3

T_2* corruption. Furthermore, it allows interleaved EPI acquisition without Nyquist ghosting artifact due to field inhomogeneity.

Several previous MRF studies already demonstrated that MRF could be further accelerated or the quality of the maps could be improved by incorporating parallel imaging techniques (6, 7). Our approach using the CG-SENSE also demonstrated improvement of the quantitative maps. Here, we achieved acceleration factor of five in k_z axis (R_z = 5) using the proposed method, although previous 3D MRF methods used R_z = 3 (18, 19, 21). This could have been accomplished by combining non-cartesian acquisition with k_z-t undersampling (43).

Because the quantitative approach provides information of the compositional changes of knee cartilage, many quantitative studies have been reported in clinical studies (25, 27, 31, 49, 50). Similar results, especially increased T_2 values in the damaged region, were also seen in the 2 patients using the proposed method. Clinical study with additional knee pain patients would be our next study plan. Furthermore, the proposed method acquired 3D T_1 and T_2 maps simultaneously. Delayed T_1 mapping with injection of the $Gd(DTPA)^{2-}$ (dGEMRIC) using the proposed method might provide volumetric high resolution GAG information as well. Applying $T_{1\rho}$ preparation module would be an alternative approach for GAG contents (51).

Although the proposed method presented good quality 3D high resolution MRF in short scan time, several challenges of MRF were not considered. For example, several MRF studies reported that motion artifact could affect the accuracy of quantification (52, 53). Because of the hybrid non-cartesian and cartesian acquisition in the proposed method, motion artifact could appear as complicated pattern. Another challenge of MRF is the effect of B_1^+ inhomogeneity. Many MRF researches already presented the B_1^+ inhomogeneity artifact and its solutions (8-10, 15, 16, 19). Therefore, these concerns should be considered when the method is applied to the motion sensitive regions or regions with large FOV (e.g., brain, abdomen, breast) or high field MRI (e.g., 7T). However, in our application of knee cartilage, both motion and B_1^+ inhomogeneity were not big issues.

A limitation of the proposed study could be the choice of the number of slices (N_z) which was not fully flexible. The number of slices should be an order of $2*N_{ETL}*R_z$, because the proposed method used centric order interleaved EPI acquisition. For example, if the parameters N_{ETL} = 4, R_z = 5 were decided for the acceleration, N_z could be 40, 80, 120, 160, and 200 slices. Another limitation of the study could be some streaking artifacts which were visible especially in the muscles around the vessel. This might be due to the strong flow effect of the femoral artery. A flow suppression preparation pulse module could be used to decrease these effects.

In conclusion, a 3D high resolution MRF method was developed with a novel hybrid radial-interleaved EPI acquisition. Both the pulse sequence and the reconstruction method were implemented for high resolution mapping within practical scan time enabling 3D PD, T_1 and T_2 maps with 0.5 mm isotropic resolution for whole coverage of knee cartilage acquired in 7 min and 10 sec. This method might be helpful for various clinical applications that require volumetric quantitative mapping with sub-millimeter resolution.

Supplementary Materials

The Figure Supplements are available with this article at https://doi.org/10.13104/imri.2021.25.3.141

Acknowledgments

This research was supported by Basic Science Research Program through the National Research Foundation of Korea (NRF) grant funded by the Korea government (MSIT) (NRF-2019R1A2C1090635) and by the advanced MR study group of KSMRM (2021).

REFERENCES

1. Ma D, Gulani V, Seiberlich N, et al. Magnetic resonance fingerprinting. Nature 2013;495:187-192
2. Jiang Y, Ma D, Seiberlich N, Gulani V, Griswold MA. MR fingerprinting using fast imaging with steady state precession (FISP) with spiral readout. Magn Reson Med 2015;74:1621-1631
3. Jiang Y, Ma D, Jerecic R, et al. MR fingerprinting using the quick echo splitting NMR imaging technique. Magn Reson Med 2017;77:979-988
4. McGivney DF, Pierre E, Ma D, et al. SVD compression for magnetic resonance fingerprinting in the time domain. IEEE Trans Med Imaging 2014;33:2311-2322
5. Pierre EY, Ma D, Chen Y, Badve C, Griswold MA. Multiscale reconstruction for MR fingerprinting. Magn Reson Med 2016;75:2481-2492
6. Asslander J, Cloos MA, Knoll F, Sodickson DK, Hennig J, Lattanzi R. Low rank alternating direction method of multipliers reconstruction for MR fingerprinting. Magn

Reson Med 2018;79:83-96
7. Lima da Cruz G, Bustin A, Jaubert O, Schneider T, Botnar RM, Prieto C. Sparsity and locally low rank regularization for MR fingerprinting. Magn Reson Med 2019;81:3530-3543
8. Buonincontri G, Sawiak SJ. MR fingerprinting with simultaneous B1 estimation. Magn Reson Med 2016;76:1127-1135
9. Ma D, Coppo S, Chen Y, et al. Slice profile and B1 corrections in 2D magnetic resonance fingerprinting. Magn Reson Med 2017;78:1781-1789
10. Cloos MA, Knoll F, Zhao T, et al. Multiparametric imaging with heterogeneous radiofrequency fields. Nat Commun 2016;7:12445
11. Korzdorfer G, Jiang Y, Speier P, et al. Magnetic resonance field fingerprinting. Magn Reson Med 2019;81:2347-2359
12. Hong T, Han D, Kim DH. Simultaneous estimation of PD, T1, T2 , T2* , and B0 using magnetic resonance fingerprinting with background gradient compensation. Magn Reson Med 2019;81:2614-2623
13. Wang CY, Coppo S, Mehta BB, Seiberlich N, Yu X, Griswold MA. Magnetic resonance fingerprinting with quadratic RF phase for measurement of T2* simultaneously with deltaf, T1 , and T2. Magn Reson Med 2019;81:1849-1862
14. Hamilton JI, Jiang Y, Chen Y, et al. MR fingerprinting for rapid quantification of myocardial T1 , T2 , and proton spin density. Magn Reson Med 2017;77:1446-1458
15. Chen Y, Jiang Y, Pahwa S, et al. MR fingerprinting for rapid quantitative abdominal imaging. Radiology 2016;279:278-286
16. Chen Y, Panda A, Pahwa S, et al. Three-dimensional MR fingerprinting for quantitative breast imaging. Radiology 2019;290:33-40
17. Ma D, Pierre EY, Jiang Y, et al. Music-based magnetic resonance fingerprinting to improve patient comfort during MRI examinations. Magn Reson Med 2016;75:2303-2314
18. Liao C, Bilgic B, Manhard MK, et al. 3D MR fingerprinting with accelerated stack-of-spirals and hybrid sliding-window and GRAPPA reconstruction. Neuroimage 2017;162:13-22
19. Ma D, Jiang Y, Chen Y, et al. Fast 3D magnetic resonance fingerprinting for a whole-brain coverage. Magn Reson Med 2018;79:2190-2197
20. Cao X, Ye H, Liao C, Li Q, He H, Zhong J. Fast 3D brain MR fingerprinting based on multi-axis spiral projection trajectory. Magn Reson Med 2019;82:289-301
21. Ma D, Jones SE, Deshmane A, et al. Development of high-resolution 3D MR fingerprinting for detection and characterization of epileptic lesions. J Magn Reson Imaging 2019;49:1333-1346
22. Burstein D, Bashir A, Gray ML. MRI techniques in early stages of cartilage disease. Invest Radiol 2000;35:622-638
23. Blumenkrantz G, Majumdar S. Quantitative magnetic resonance imaging of articular cartilage in osteoarthritis. Eur Cell Mater 2007;13:76-86
24. Crema MD, Roemer FW, Marra MD, et al. Articular cartilage in the knee: current MR imaging techniques and applications in clinical practice and research. Radiographics 2011;31:37-61
25. Choi JA, Gold GE. MR imaging of articular cartilage physiology. Magn Reson Imaging Clin N Am 2011;19:249-282
26. Dardzinski BJ, Mosher TJ, Li S, Van Slyke MA, Smith MB. Spatial variation of T2 in human articular cartilage. Radiology 1997;205:546-550
27. Mosher TJ, Dardzinski BJ, Smith MB. Human articular cartilage: influence of aging and early symptomatic degeneration on the spatial variation of T2--preliminary findings at 3 T. Radiology 2000;214:259-266
28. Mosher TJ, Smith H, Dardzinski BJ, Schmithorst VJ, Smith MB. MR imaging and T2 mapping of femoral cartilage: in vivo determination of the magic angle effect. AJR Am J Roentgenol 2001;177:665-669
29. Dardzinski BJ, Laor T, Schmithorst VJ, Klosterman L, Graham TB. Mapping T2 relaxation time in the pediatric knee: feasibility with a clinical 1.5-T MR imaging system. Radiology 2002;225:233-239
30. Maier CF, Tan SG, Hariharan H, Potter HG. T2 quantitation of articular cartilage at 1.5 T. J Magn Reson Imaging 2003;17:358-364
31. Dunn TC, Lu Y, Jin H, Ries MD, Majumdar S. T2 relaxation time of cartilage at MR imaging: comparison with severity of knee osteoarthritis. Radiology 2004;232:592-598
32. Mosher TJ, Dardzinski BJ. Cartilage MRI T2 relaxation time mapping: overview and applications. Semin Musculoskelet Radiol 2004;8:355-368
33. Burstein D, Velyvis J, Scott KT, et al. Protocol issues for delayed Gd(DTPA)(2-)-enhanced MRI (dGEMRIC) for clinical evaluation of articular cartilage. Magn Reson Med 2001;45:36-41
34. Tiderius CJ, Olsson LE, Leander P, Ekberg O, Dahlberg L. Delayed gadolinium-enhanced MRI of cartilage (dGEMRIC) in early knee osteoarthritis. Magn Reson Med 2003;49:488-492
35. Williams A, Gillis A, McKenzie C, et al. Glycosaminoglycan distribution in cartilage as determined by delayed gadolinium-enhanced MRI of cartilage (dGEMRIC): potential clinical applications. AJR Am J Roentgenol 2004;182:167-172
36. Tiderius CJ, Svensson J, Leander P, Ola T, Dahlberg L.

dGEMRIC (delayed gadolinium-enhanced MRI of cartilage) indicates adaptive capacity of human knee cartilage. Magn Reson Med 2004;51:286-290
37. Cloos MA, Asslander J, Abbas B, et al. Rapid radial T1 and T2 mapping of the hip articular cartilage with magnetic resonance fingerprinting. J Magn Reson Imaging 2019;50:810-815
38. Pruessmann KP, Weiger M, Scheidegger MB, Boesiger P. SENSE: sensitivity encoding for fast MRI. Magn Reson Med 1999;42:952-962
39. Pruessmann KP, Weiger M, Bornert P, Boesiger P. Advances in sensitivity encoding with arbitrary k-space trajectories. Magn Reson Med 2001;46:638-651
40. Winkelmann S, Schaeffter T, Koehler T, Eggers H, Doessel O. An optimal radial profile order based on the Golden Ratio for time-resolved MRI. IEEE Trans Med Imaging 2007;26:68-76
41. Mugler JP 3rd. Improved three-dimensional GRASE imaging with the SORT phase-encoding strategy. J Magn Reson Imaging 1999;9:604-612
42. Uecker M, Lai P, Murphy MJ, et al. ESPIRiT--an eigenvalue approach to autocalibrating parallel MRI: where SENSE meets GRAPPA. Magn Reson Med 2014;71:990-1001
43. Wright KL, Hamilton JI, Griswold MA, Gulani V, Seiberlich N. Non-Cartesian parallel imaging reconstruction. J Magn Reson Imaging 2014;40:1022-1040
44. The Berkeley Advanced Reconstruction Toolbox (BART) toolbox (https://mrirecon.github.io/bart/). Published 2015. Accessed June 9, 2021
45. Deoni SC, Peters TM, Rutt BK. High-resolution T1 and T2 mapping of the brain in a clinically acceptable time with DESPOT1 and DESPOT2. Magn Reson Med 2005;53:237-241
46. Ben-Eliezer N, Sodickson DK, Block KT. Rapid and accurate T2 mapping from multi-spin-echo data using Bloch-simulation-based reconstruction. Magn Reson Med 2015;73:809-817
47. Outerbridge RE. The etiology of chondromalacia patellae. J Bone Joint Surg Br 1961;43-B:752-757
48. Cruz G, Schneider T, Bruijnen T, Gaspar AS, Botnar RM, Prieto C. Accelerated magnetic resonance fingerprinting using soft-weighted key-hole (MRF-SOHO). PLoS One 2018;13:e0201808
49. Li X, Benjamin Ma C, Link TM, et al. In vivo T(1rho) and T(2) mapping of articular cartilage in osteoarthritis of the knee using 3 T MRI. Osteoarthritis Cartilage 2007;15:789-797
50. Wiener E, Pfirrmann CW, Hodler J. Spatial variation in T1 of healthy human articular cartilage of the knee joint. Br J Radiol 2010;83:476-485
51. Li X, Han ET, Ma CB, Link TM, Newitt DC, Majumdar S. In vivo 3T spiral imaging based multi-slice T(1rho) mapping of knee cartilage in osteoarthritis. Magn Reson Med 2005;54:929-936
52. Mehta BB, Ma D, Pierre EY, Jiang Y, Coppo S, Griswold MA. Image reconstruction algorithm for motion insensitive MR Fingerprinting (MRF): MORF. Magn Reson Med 2018;80:2485-2500
53. Yu Z, Zhao T, Asslander J, Lattanzi R, Sodickson DK, Cloos MA. Exploring the sensitivity of magnetic resonance fingerprinting to motion. Magn Reson Imaging 2018;54:241-248